

# DEIMOS Spectroscopy of Star-Forming Galaxies in the *AKARI* North Ecliptic Pole-Deep Field

HELEN K. KIM,<sup>1</sup> MATTHEW A. MALKAN,<sup>1</sup> NAGISA OI,<sup>2</sup> DENIS BURGARELLA,<sup>3</sup> VERONIQUE BUAT,<sup>3</sup>  
TOSHINOBU TAKAGI,<sup>4</sup> AND HIDEO MATSUHARA<sup>4</sup>

<sup>1</sup>*Department of Physics and Astronomy, University of California, Los Angeles, CA 90095-1547, USA*

<sup>2</sup>*Tokyo University of Science, 1-3 Kagurazaka, Shinjuku-ku, Tokyo 162-8601, Japan*

<sup>3</sup>*Aix-Marseille Université, CNRS - LAM (Laboratoire d'Astrophysique de Marseille) UMR 7326, 13388 Marseille, France*

<sup>4</sup>*Institute of Space and Astronautical Science, Japan Aerospace Exploration Agency, 3-1-1 Yoshinodai, Chuo-ku, Sagamihara 252-5210, Japan*

## ABSTRACT

We present follow-up optical DEIMOS/Keck-II spectra of  $\sim 180$  galaxies (median  $z \sim 0.7$ ) in the *AKARI* NEP-Deep field. The spectroscopic redshifts ( $z_{\text{spec}}$ ) agree well with photometric redshifts ( $z_{\text{phot}}$ ) at  $z < 1$ , with mean  $|z| \approx 0.07$ , but the photometric redshifts are systematically too high at  $z > 1$ . One Seyfert 1.9 and one Seyfert 2 were identified from their emission lines, but no LINERs were found, in contrast to [Kartaltepe et al. \(2015\)](#), 84% of our objects are classified to be along the star-forming, H II sequence. At a given stellar mass, gas phase metallicities were found to be 0.1–0.2 dex lower than the local SDSS relation, but consistent with the relation found by [Zahid et al. \(2011\)](#) at  $z \sim 0.8$ . Gas reddenings were derived from Balmer emission line ratios. In the majority of cases, the corresponding extinction at  $H\alpha$  is  $\sim 1$  mag, typical of normal spiral galaxies. Star formation rates (SFRs) were estimated from the luminosities of either [O II] $\lambda 3727$  or  $H\alpha$ , and agreed reasonably (50% scatter). In galaxies with equivalent width  $\text{EW}(H\alpha)$  of  $10 \text{ \AA}$  or less, the broadband spectral energy distribution (SED) fitting significantly overestimates the SFR.

**Keywords:** techniques: spectroscopic – galaxies: evolution; distances and redshifts – infrared: galaxies

## 1. INTRODUCTION

The extragalactic background suggests at least half the luminous energy generated by stars has been reprocessed into the infrared (IR) by dust ([Lagache et al. 1999](#)), and that dust-obscured star formation was more important at higher redshifts than today ([Buat et al. 2007](#)). However, the individual dusty galaxies producing this IR light are not well understood, partly due to the requirement of deep wide-field mid-IR surveys to find them, and then the extreme difficulty of studying their dust spectra. The only mission to overcome those limitations was the Japanese *AKARI* Infrared Camera (IRC), which mapped the  $\sim 0.5$  sq. deg North Ecliptic Pole (NEP)-Deep field (Figure 1 in [Tateuchi et al. 2012](#)) from 2–24  $\mu\text{m}$ . Follow-up optical spectroscopy is valuable for several goals: (1) to test uncertain photometric redshifts of IRC spectra at  $z \sim 0.8$ –1.5, (2) find emission line evidence of active galactic nuclei (AGN) in substantially reddened galaxies, (3) measure metallicity diagnostics, (4) provide an estimate of the less-obscured SFR based on the [O II] luminosity ([Ly et al. 2012](#)) and compare against our IR estimates of total (obscured) SFR, (5) measure gas extinctions in galaxies with strong emission lines.

## 2. SAMPLE SELECTION AND OBSERVATIONS

The NEP-Deep field was subsequently observed very intensively at all other wavelengths from the radio to the UV and X-rays. With nearly 10,000 galaxies detected by the IRC in the NEP-Deep, we prioritized  $R > 22.5$  galaxies with higher photometric redshifts ( $z_{\text{phot}} \sim 1$ ), with MIR detections (9 and/or 18  $\mu\text{m}$ ), and with power-law spectra suggestive of AGN components, or which are counterparts to *Chandra*-detected X-ray sources. In August 2014, September 2015, and September 2016, we observed five slitmasks with DEep Imaging Multi-Object Spectrograph (DEIMOS; [Faber et al. 2003](#)) on Keck II/W. M. Keck Observatory for two hours each. The observing conditions for the masks were generally clear and dry with 0''6–0''8 seeing, and a 900 lines/mm ZD grating was used. We reduced the raw DEIMOS spectra with the DEEP2 spec2d reduction pipeline ([Cooper et al. 2012](#); [Newman et al. 2013](#)). Including serendipitous sources, the total number of obtained spectra ranged from  $\sim 110$ –200 per mask, and successful detections ranged from  $\sim 1/5$ – $1/3$ . The mask with the

fewest detections had significantly more serendipitous sources and lower signal-to-noise. Thus, our final sample contains 185 objects for which we were able to measure  $z_{\text{spec}}$ . The spectra were flux-calibrated based on the slitmask alignment stars, where the stars' ( $V - J$ ) colors were used to determine the spectral type and the source spectra were divided by the blackbody continuum, which was normalized to the stars' broadband magnitudes (Figure 1 left panel).

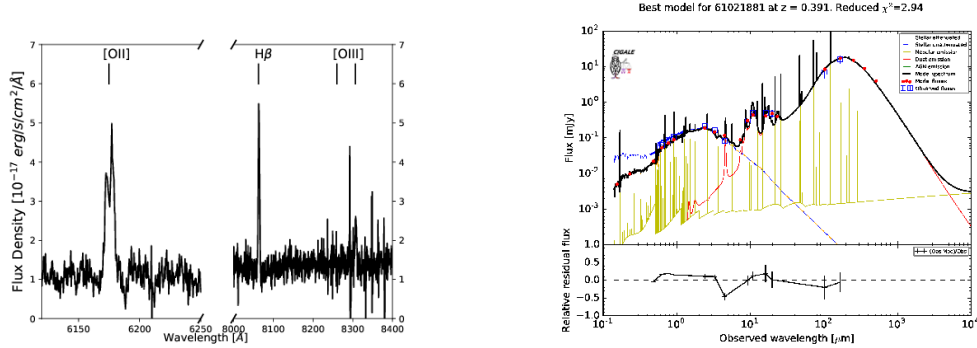


**Figure 1.** Left: Example of a typical flux-calibrated spectrum at  $z_{\text{spec}} = 0.658$ . The dashed lines identify, in order of increasing wavelength, [O II] $\lambda$ 3727, H $\beta$ , and [O III] $\lambda$ 4959,5007. Right: Example CIGALE SED fit of a typical star-forming galaxy, including data from 13 photometric bands.

### 3. REDSHIFT MEASUREMENTS AND SPECTRAL ENERGY DISTRIBUTION

We measured  $z_{\text{spec}}$  using a combination of Specpro (Masters & Capak 2011), to visually determine an initial redshift guess, and a centroid procedure that we developed. We fit Gaussians with a linear continuum using MPFIT (Markwardt 2009). [O II] $\lambda$ 3727 was fit with either a single (unresolved) or double Gaussian (resolved). For [N II] and H $\alpha$ , we applied a triple Gaussian fit with the amplitude of [N II] $\lambda$ 6583 set to be three times larger than that of [N II] $\lambda$ 6548, and a double Gaussian fit for [S II]. The H $\gamma$  line often showed a dip in the continuum due to underlying stellar absorption, and in these cases we manually adjusted the continuum to compensate for the absorption. Figure 2(a) shows the redshift distribution for our sample where at least one line was detected. In cases where only a single line was detected, we identified it as [O II] (at  $z \sim 1$ ), provided a photometric redshift was available, and assigned an uncertainty of  $\Delta z_{\text{spec}} = 0.001$ . In Figure 2(b), we compare our measured  $z_{\text{spec}}$  to the  $z_{\text{phot}}$  (Oi et al. 2014). The  $z_{\text{spec}}$  agree well with  $z_{\text{phot}}$  at  $z < 1$ , with mean  $|\Delta z| \approx 0.07$ . However at  $z > 1$ ,  $z_{\text{phot}}$  are systematically too high, with mean  $|\Delta z| \approx 0.18$ . This may result from strong emission lines (e.g., large black stars show  $\text{EW}_{\text{rest}}([\text{O II}]) \sim 100 \text{ \AA}$ ) and lack of H-band photometry in the SED fitting where the Balmer break at  $\sim 6500 \text{ \AA}$  is poorly sampled. A catastrophic failure can also result from the LePhare procedure misidentifying the Balmer break as the Lyman break for faint, reddened galaxies and/or galaxies with noisy photometry; however, this is not the primary source of error for where most of our targets are at  $z_{\text{spec}} < 1.4$ .

Modeling a galaxy's SED depends critically on having an accurate redshift in order to deduce the rest-frame wavelength and thus infer the origin of important spectral features, such as PAHs (e.g., Takagi et al. 2012). Using our  $z_{\text{spec}}$  as inputs, Burgarella et al. modeled SEDs for a subset of the detected sources with CIGALE (Figure 1, right; Roehly et al. 2012). The output parameters that we use in the following analyses include the stellar mass ( $M_*$ ), SFR, and extinction  $A_V$ .

From the emission line EW, we also calculated the full-width half-maximum (FWHM), where  $\text{FWHM} = 2\sqrt{2 \ln 2} \sigma$ , and the velocity dispersion of the lines:  $\Delta v = c \times \frac{\text{FWHM}}{\lambda_{\text{em}}(1+z)}$ . Figure 2(c) shows dynamical mass estimates for a subset of our galaxies, where  $\Delta v$  was averaged per object. There is a clear trend of higher  $\Delta v$  ( $\sim 500 \text{ km/s}$ ) for more massive systems.

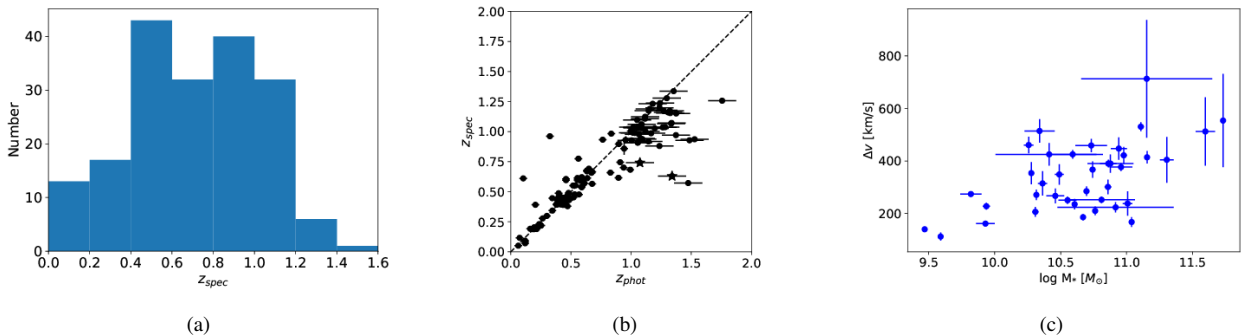


**Figure 2.** (a) Distribution of detected spectroscopic redshifts in our sample, with median  $z \sim 0.7$ . (b) Comparison of spectroscopic vs. photometric redshifts for all detections. The dashed line shows the expected relation for a perfect correlation. The star symbols denote the objects with  $\text{EW}([\text{O II}]) \sim 100 \text{ \AA}$ . (c) Dynamical mass estimates for a subset of our galaxies.

#### 4. GALAXY CLASSIFICATION AND METALLICITY

The nebular emission lines provide information about a galaxy’s star formation, AGN contribution, metallicity, dust extinction, temperature, electron number density, among other properties. In Figure 3, we present the two most prominent versions of the Baldwin-Phillips-Terlevich (BPT) diagram (Baldwin et al. 1981). BPT-NII compares  $[\text{O III}]/\text{H}\beta$  to  $[\text{N II}]/\text{H}\alpha$ , while BPT-SII compares against  $[\text{S II}]/\text{H}\alpha$ . Our 19 targets on the BPT diagram consist mainly (84%) of normal, H II star-forming galaxies along the Ka03 classification line. We also identify two strong Seyfert galaxies (11%) and one weak Seyfert/composite galaxy (5%) found between the Ke01 and Ka03 lines. The Seyfert 1.9 has X-ray emission detected from deep *Chandra* observations, but the Seyfert 2 is not X-ray detected, although its mid-IR SED does show the hot dust characteristic of a Seyfert nucleus. For comparison, we overplot NEP DEIMOS data from T. Takagi and T. Wada (2009), whose sample of 310 detected galaxies are at lower  $z$  (median  $z_{\text{spec}} = 0.54$ ) and thus brighter; 70 of these objects are on the BPT. No LINERs were found in our sample, in contrast to Kartaltepe et al. (2015), who found that  $>2/3$  of the highly luminous  $24\ \mu\text{m}$ -selected galaxies at  $z \sim 0.7$  from the FMOS-COSMOS survey lie to the right of the star-forming/H II sequence. The authors interpret this to mean that the majority of LIRGs and ULIRGs at  $z \sim 1$  are either AGN-dominated or AGN/star-forming composites, which is much higher than the  $\sim 15\text{--}20\%$  estimates from previous observations of local *IRAS*-selected galaxies made by our collaborators and others (Harwit et al. 1987). However, we need more data at  $z \sim 1$  in order to better quantify the origin of energy production in IR-luminous galaxies.

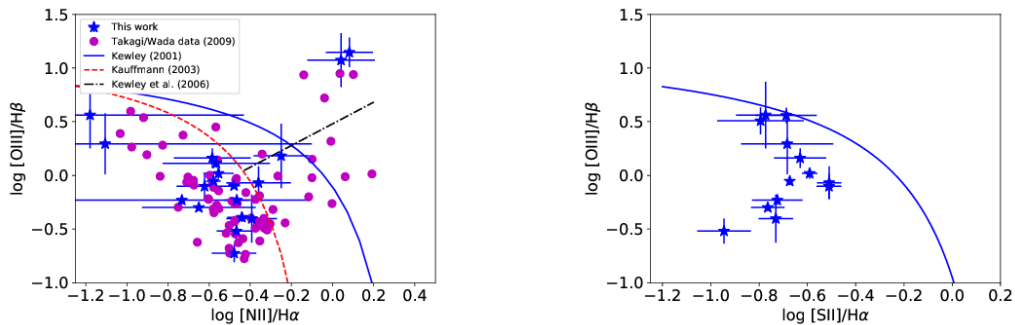


**Figure 3.** BPT-NII (left) and SII (right) diagrams. The Kewley (2001) (Ke01) solid classification line is used to identify extreme starbursts, while the Kauffmann (2003) (Ka03) dashed line is used to classify normal star formation; the Kewley et al. (2006) dash-dotted line separates Seyferts and LINERs. DEIMOS data from T. Takagi and T. Wada (2009) are overplotted for BPT-NII.

As a measurement of the gas-phase oxygen abundance, we calculate the dust-corrected  $R_{23}$  ratio, which has been commonly used in the literature to calibrate metallicity based on the strong nebular emission lines (Pagel et al. 1979). 12 of our objects had  $R_{23}$  values, ranging from approximately 2.7–12.0. However, since the  $R_{23}$  parameter is known to be degenerate with metallicity, we also calculate metallicity using  $[\text{N II}]/\text{H}\alpha$ , given by Pettini & Pagel (2004):  $12 + \log(\text{O}/\text{H}) = 8.90 + 0.57 \log([\text{N II}]/\text{H}\alpha)$ . For the 17 objects with  $[\text{N II}]/\text{H}\alpha$ , we find that  $12 + \log(\text{O}/\text{H})$  ranges from 8.5–8.9. Partially as a result of  $R_{23}$ ’s dependence on flux calibrated lines, only four of our objects have both measured  $R_{23}$  and  $[\text{N II}]/\text{H}\alpha$ , so our comparison between the two metallicity calibrations is limited. However, we find no significant correlation for these objects. Based on their  $[\text{O III}]/\text{H}\beta$  flux ratios, the normal galaxies on our BPT diagram range from fairly massive systems with average metals to quite metal rich systems. The sources with elevated  $[\text{O III}]/\text{H}\beta$  signify either low-mass, metal-poor dwarf galaxies or the presence of a Seyfert component. We find the  $R_{23}$  relation to be consistent in showing objects that do not have a significantly high metallicity, in agreement with Zahid et al. (2011). After applying the PP04-T04 metallicity calibration (Kewley & Ellison 2008), we plot the  $M_*$ - $Z$  relation given by  $[\text{N II}]/\text{H}\alpha$ . Figure 4(a) shows that our galaxies are systematically lower by 0.1–0.2 dex than the Tremonti et al. (2004) positive correlation for local SDSS galaxies, with our galaxies favoring weaker  $[\text{N II}]$  for these massive systems. In Figure 4(b), we compare the dust-corrected  $O_{32}$  vs.  $R_{23}$  ratios as a measure of the ionization. Our galaxies show a range of ionization, with a possible trend for either metals to decrease, or ionization to increase at higher  $z$ .

#### 5. DUST EXTINCTION AND STAR FORMATION RATE

The Balmer decrement represents the amount of reddening in a galaxy due to dust extinction and must be considered when measuring a galaxy’s intrinsic SFR. We calculated the observed excess  $E(\beta - \alpha)$  with the observed  $\text{H}\alpha/\text{H}\beta$  or  $\text{H}\gamma/\text{H}\beta$  line fluxes and a theoretical value of 2.86 and 0.47 for the respective Balmer decrements, assuming case B recombination at  $T = 10^4$  K,  $n_e \sim 10^2\text{--}10^4\ \text{cm}^{-3}$  (Osterbrock et al. 1989). We assume a Cardelli attenuation curve in order to deduce  $E(B - V)$  and  $A_{3727}$  (Cardelli et al. 1989). Most of our values for extinction  $A(\text{H}\alpha)$  range from 1–2 magnitudes. However, for the normal galaxies, CIGALE tends to put our objects at the low end of our Balmer decrement at 1 mag. For *Chandra* X-ray sources, CIGALE overestimates the extinction (e.g., by a factor of four for one source) and underestimates the IR-detected AGN extinction by a factor of two.

In order to derive a SFR, we measured the line luminosities of sources with  $\text{H}\alpha$  and  $[\text{O II}]$ . We apply the SFR- $L_{\text{H}\alpha}$  relation from Kennicutt et al. (2009):  $\text{SFR}_{\text{H}\alpha} [M_{\odot}\ \text{yr}^{-1}] = 5.49 \times 10^{-42} L_{\text{H}\alpha}$  (erg  $\text{s}^{-1}$ ) and the SFR- $L_{[\text{O II}]}$  relation from

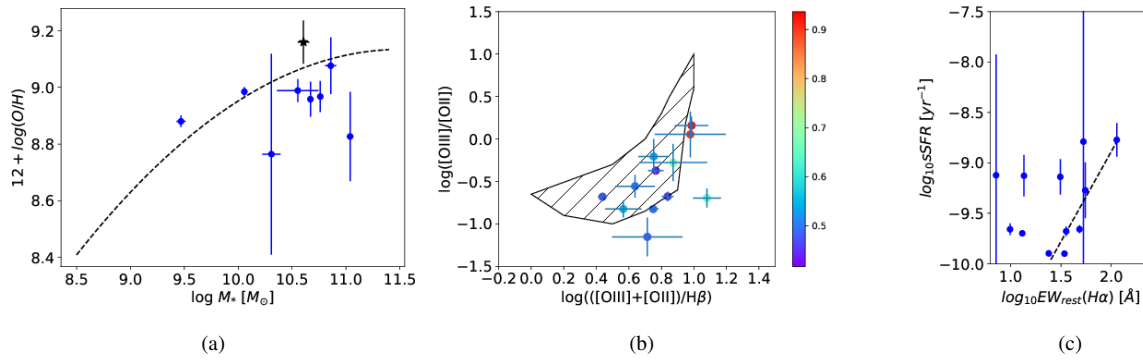


**Figure 4.** (a) Mass-metallicity relation from  $[\text{N II}]/\text{H}\alpha$ , with Tremonti et al. (2004) local SDSS galaxy population (dashed line). Blue dots are for star-forming galaxies and black star for the SF/AGN composite galaxy. (b) Dust-corrected  $O_{32}$  vs.  $R_{23}$  diagram. Redshifts range from  $0.42 < z < 0.94$ , represented by the color bar. Hatched polygon represents the dust-corrected SDSS local population. (c) Specific star formation rate derived by CIGALE vs. observed rest-frame  $\text{H}\alpha$  EW. Dotted line is to guide the eye and is not a fit.

Kewley et al. (2004):  $\text{SFR}_{[\text{O II}]} [M_{\odot} \text{ yr}^{-1}] = 6.58 \times 10^{-42} L_{[\text{O II}]} (\text{erg s}^{-1})$ , where the luminosities have been corrected for extinction. We find the SFRs based on these two emission line calibrations to be in reasonable agreement within a factor of  $\sim 2$ . Because the EW of  $\text{H}\alpha$  can be used as a proxy for star formation, we compare it against the specific star formation rate derived from the SFR and  $M_{*}$  from CIGALE in Figure 4(c). As shown by the dotted line, the  $\text{H}\alpha$  emission line sSFRs agree reasonably with CIGALE continuum fits when the lines are strong, but in galaxies with  $\text{EW}(\text{H}\alpha) < 10 \text{ \AA}$ , CIGALE significantly overestimates the star formation rate.

## ACKNOWLEDGMENTS

This research is based on observations with *AKARI*, a JAXA project with the participation of ESA. The analysis pipeline used to reduce the DEIMOS data was developed at UC Berkeley with support from NSF grant AST-0071048.

## REFERENCES

- Baldwin, J. A., Phillips, M. M., Terlevich, R. 1981, PASP, 93, 5B  
 Buat, V., Takeuchi, T. T., Iglesias-Páramo, J. et al. 2007, ApJS, 173, 404B  
 Cardelli, J. A., Clayton, G. C., & Mathis, J. S. 1989, ApJ, 345, 245C  
 Cooper, M. C., Newman, J. A., Davis, M. et al. 2012, Astrophysics Source Code Library, ascl:1203.003  
 Faber, S. M., Phillips, A. C., Kibrick, R. I. et al. 2003, SPIE, 4841, 1657F  
 Harwit, M., Houck, J. R., Soifer, B. T. et al. 1987, NASCP, 2466, 387H  
 Kartaltepe, J. S., Sanders, D. B., Silverman, J. D. et al. 2015, ApJL, 806L, 35K  
 Kauffmann, G. 2003, MNRAS, 346, 1055K  
 Kennicutt, R. C., Jr., Hao, C.-N., Calzetti, D. et al. 2009, ApJ, 703, 1672K  
 Kewley, L. J. and Ellison, S. L., 2008, ApJ, 681, 1183K  
 Kewley, L. J., Geller, M. J., Jansen, R. A. 2004, AJ, 127, 2002K  
 Kewley, L. J., Groves, B., Kauffmann, G., & Heckman, T. 2006, MNRAS, 372, 961  
 Kewley, L. J. 2001, ApJ, 556, 121K  
 Lagache, G., Abergel, A., Boulanger, F. et al. 1999, A&A, 344, 322L  
 Ly, C., Malkan, M. A., Kashikawa, N. et al. 2012, ApJ, 757, 63L  
 Markwardt, C.-B. 2009, Astronomical Data Analysis Software and Systems XVIII, 411, 251  
 Masters D. & Capak P., 2011, PASP, 123, 638M  
 Newman, J. A., Cooper, M. C., Davis, M. et al. 2013, ApJS, 208, 5N  
 Oi, N., Matsuhara, H., Murata, K. et al. 2014, A&A, 566A, 600  
 Osterbrock, D. E. 1989, Annals of the New York Academy of Sciences, 571, 990  
 Pagel, B. E. J., Edmunds, M. G., Blackwell, D. E., Chun, M. S., & Smith, G. 1979, MNRAS, 189, 95  
 Pettini, M. & Pagel, B. E. J. 2004, MNRAS, 348L, 59P  
 Roehlly, Y., Burgarella, D., Buat, V. et al. 2012, ASPC, 461, 569R  
 Takagi, T., Matsuhara, H., Goto, T. et al. 2012, A&A, 537A, 24T  
 Tateuchi K., Motohara K., Konishi M. et al. 2012, PKAS, 27, 297T  
 Tremonti, C. A., Heckman, T. M., Kauffmann, G. et al. 2004, ApJ, 613, 898T  
 Zahid, H. J., Kewley, L. J., Bresolin, F., 2011, ApJ, 730, 137Z